

Article

Multiscale patterning of a metallic glass using sacrificial imprint lithography

Jonathan P. Singer¹, Candice I. Pelligra², Noga Kornblum², Youngwoo Choo³, Manesh Gopinadhan³, Punnathat Bordeenithikasem⁴, Jittisa Ketkaew⁴, Seng Fatt Liew⁵, Hui Cao⁵, Jan Schroers⁶ and Chinedum O. Osuji³

Bulk metallic glasses (BMGs) have been developed as a means to achieve durable multiscale, nanotextured surfaces with desirable properties dictated by topography for a multitude of applications. One barrier to this achievement is the lack of a bridging technique between macroscale thermoplastic forming and nanoimprint lithography, which arises from the difficulty and cost of generating controlled nanostructures on complex geometries using conventional top-down approaches. This difficulty is compounded by the necessary destruction of any resulting reentrant structures during rigid demolding. We have developed a generalized method to overcome this limitation by sacrificial template imprinting using zinc oxide (ZnO) nanostructures. It is established that such structures can be grown inexpensively and quickly with tunable morphologies on a wide variety of substrates out of solution, which we exploit to generate the nanoscale portion of the multiscale pattern through this bottom-up approach. In this way, we achieve metallic structures that simultaneously demonstrate features from the macroscale down to the nanoscale, requiring only the top-down fabrication of macro/microstructured molds. Upon detachment of the formed part from the multiscale molds, the ZnO remains embedded in the surface and can be removed by etching in mild conditions to both regenerate the mold and render the surface of the BMGs nanoporous. The ability to pattern metallic surfaces in a single step on length scales from centimeters down to nanometers is a critical step toward fabricating devices with complex shapes that rely on multiscale topography for their intended functions, such as biomedical and electrochemical applications.

Keywords: bulk metallic glasses; nanoimprint; multiscale structures; optical properties

Microsystems & Nanoengineering (2015) 1, 15040; doi:10.1038/micronano.2015.40; Published online: 21 December 2015

INTRODUCTION

Bulk metallic glasses (BMGs) are alloys in which amorphous structures can be achieved in millimeter scale or larger using modest cooling rates. BMGs possess attractive properties relative to crystalline alloys, including strength and elasticity, which are often paired with high corrosion resistance^{1,2}. BMGs have been advanced as a means to achieve metallic surfaces with multiscale textures due to their ability to be thermoplastically formed on various length scales by compression^{3,4} or blow molding⁵. In particular, the ability to thermoplastically form BMGs on the nanoscale⁶ has yielded surfaces possessing superior properties, such as high surface area, that are useful for a multitude of applications, including durable electrochemical surfaces^{7,8}, fuel cells⁹, controlled wetting surfaces¹⁰, and cellular response-manipulating patterns¹¹.

Existing methods to fabricate nanostructured metallic surfaces possess considerable limitations. For example, laser treatment^{12,13}, shock forming¹⁴, and thermoplastic forming against anodized aluminum oxide (AAO)⁶ exhibit difficulties with producing complex, non-planar geometries. There are also limitations on the final surface composition and crystal structure, such as those present with electrochemical dealloying^{15–17}. Although thermoplastic forming against silicon masters is a well-established method of generating BMG micro/nanostructures⁶, it would require a potentially large number of costly lithographic steps for the generation

of such multiscale molds, which would make single-use molding impractical. The ubiquitous alternative route of using elastomeric replicas as a flexible transfer method for micro/nanoembossing¹⁸ is incompatible with forming nanostructures in highly viscous (10^6 – 10^9 Pa-s) BMG melts due to mechanical collapse of the nanostructures on the replica, although the resulting deformation in such structures on the microscale was recently exploited to generate multiscale macro/microstructured BMGs¹⁹. In fact, the only replica material that has successfully been utilized to nanopattern BMGs is a higher temperature BMG^{6,20}. Excluding any issues with the master, forming against a multiscale BMG replica would mechanically bond the two rigid structures upon cooling, making their separation impossible without damage.

We demonstrate here a generalized, scalable method of sacrificial template imprinting of multiscale structures in a single forming step. Using zinc oxide (ZnO) nanostructures as sacrificial templates, we achieved metallic structures of a Pt-based BMG (Pt_{57.5}Cu_{14.7}Ni_{5.3}P_{22.5}), simultaneously possessing features from the macroscale down to the nanoscale. Such structures offer the ability to impart topographically controlled properties to designer BMG macro/microstructures. Although the resulting structures do not allow for exact control over the morphology, the effective medium properties, which are highly relevant to a wide variety of applications, can be tuned by highly repeatable modifications to the growth parameters.

¹Department of Mechanical and Aerospace Engineering, Rutgers University, Piscataway, NJ 08854, USA; ²Department of Chemical and Environmental Engineering, Yale University, New Haven, CT 06511, USA; ³Department of Chemical and Environmental Engineering, Center for Research on Interfacial Phenomena, Yale University, New Haven, CT 06511, USA; ⁴Department of Mechanical Engineering and Materials Science, Yale University, New Haven, CT 06511, USA; ⁵Department of Applied Physics, Yale University, New Haven, CT 06511, USA and ⁶Department of Mechanical Engineering and Materials Science, Center for Research on Interfacial Phenomena, Yale University, New Haven, CT 06511, USA

Correspondence: Chinedum O. Osuji (chinedum.osuji@yale.edu)

Received: 15 July 2015; revised: 16 November 2015; accepted: 17 November 2015

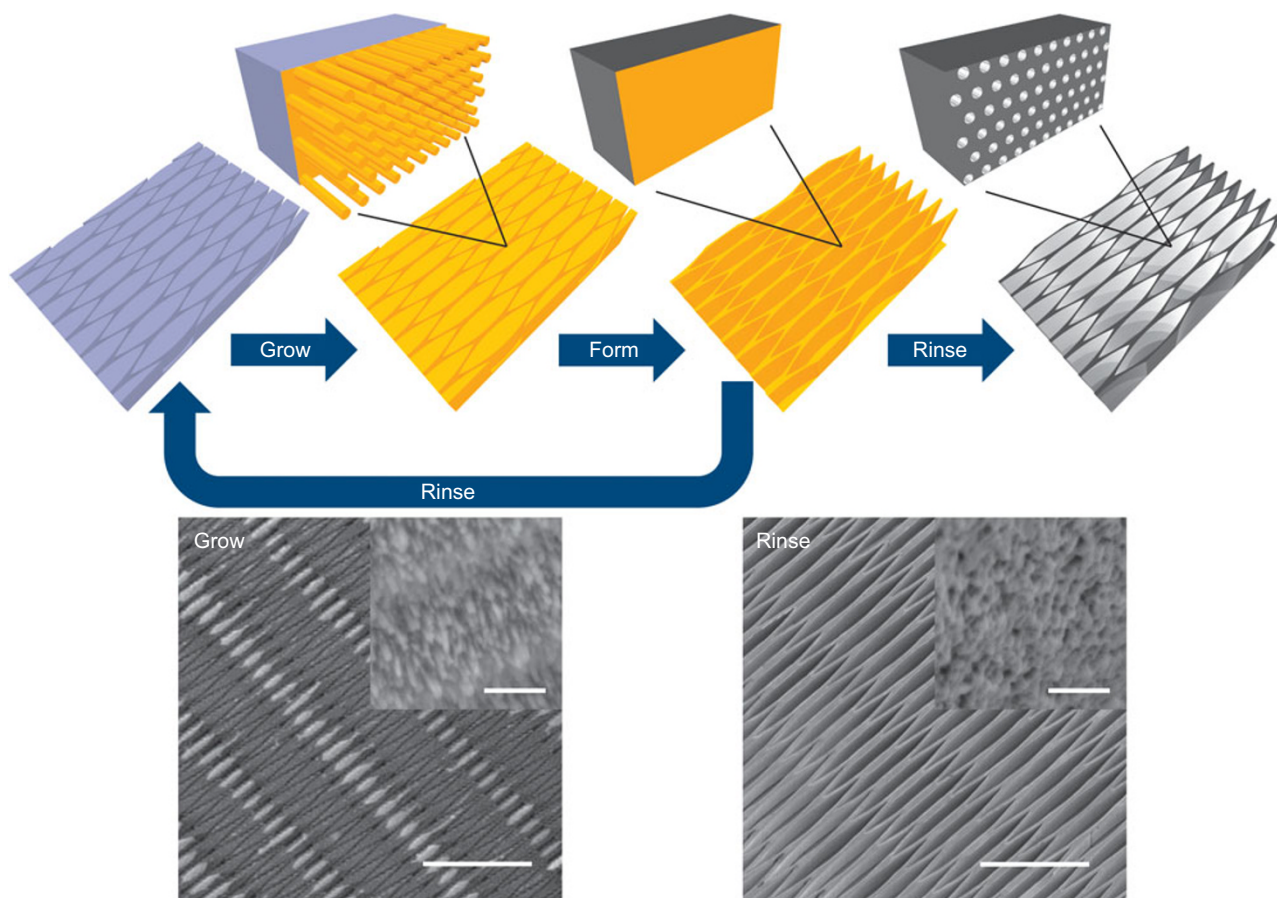


Figure 1 Formation of a 3D nano/microstructured architecture by sacrificial templating. Top: process shown schematically. A macro/microstructured mold undergoes cyclical steps of (i) nanostructure growth by, in this study, hydrothermal growth of ZnO, (ii) multiscale imprinting through thermoplastic forming of BMG in heated platens, (iii) mechanical detachment from the mold, removing both the BMG and ZnO nanomaterials embedded in the surface of the BMG, and (iv) rinsing of the mold, here in 0.1 M acetic acid, to remove the nanostructures. Each cycle generates a molded part that can be subsequently rinsed in the same manner for removal of the sacrificial materials. Bottom: SEM images with high magnification insets of (left) a fabricated multiscale mold after growth of the sacrificial nanostructures and (right) the final rinsed multiscale BMG structure of a textured stent geometry. All images imaged at a 30° tilt. Scale bars at 200 μm in main images and 200 nm in insets.

The developed method is shown schematically along with a fabricated stent-like architecture in Figure 1. The macro/microscale aspects of the mold can be machined or microfabricated using standard tools, on the one hand. The nanoscale portions, on the other hand, are instead grown on the surface of the mold. The BMG is then formed against the patterned mold with the intention that the grown nanoscale structures will be embedded into the surface of the BMG. The nanostructures are then removed from the mold either during detachment or by a subsequent rinsing step. This step is the key feature of this approach; in contrast to conventional nanoimprint lithography whereby fine, high-aspect ratio molds or mold features are the most costly, in sacrificial imprint, they are the least expensive portion of the structure and are designed to be destroyed during processing. This feature is critical for the scalable incorporation of nanostructured surfaces into three-dimensional (3D) multiscale devices; it also avoids the issue of resist fracture that is ubiquitous in thermal nanoimprinting²¹, whereby thermal expansion mismatch leads to gripping of the structures during cooling and subsequent failure by tear-away of either the imprinted material or the mold. Avoiding damage to the resist is particularly problematic in high-aspect ratio structures due to the nature of stress concentration. The use of a 'break-away' interface also reduces the need for surface functionalization to assist with the

surface energy cost of the demolding process. By mitigating these concerns, the sensitivity of the patterning to the thermal history during processing is greatly reduced.

Compared with currently employed methods of nanofabrication, such as forming into AAO molds or nanopatterned silicon, our strategy greatly reduces the costs of mold fabrication (compared with silicon), enables reentrant nanostructures, and enables patterning of non-planar surfaces, which are extremely difficult in conventional silicon etching and lead to complicated electric field distributions in AAO formation thus limiting maximum curvature variation^{22–24}. Our strategy also widens the possible selection of mold materials to include those that are usually impractical for 3D nanopatterning (e.g., machined metal molds). Considered generally, the sacrificial template can be freely selected from any nanomaterial; however, hydrothermally grown ZnO nanomaterials present a range of desirable properties for the process: (i) it is widely established that such structures can be grown with tunable morphologies on a wide variety of substrates in an inexpensive manner^{25–27}; (ii) hydrothermal growth is performed through an immersion-based deposition that is batch-scalable; (iii) ZnO can be rapidly etched in a mild acid or base (Supplementary Figure S1), which has led to past applications in templating^{28,29}; (iv) the growth process utilizes mild, aqueous conditions and inexpensive reagents; and (v) ZnO itself

is a highly functional material possessing desirable transport and piezoelectric properties³⁰. The suitability of BMG alloys for this method depends on (i) the alloys' formability, (ii) its wetting on ZnO, and (iii) its tendency to oxidize³¹. Here, we focused on a highly formable Pt-alloy; however, the method is generally applicable to other formable systems such as Pd- or Ni-based alloys (Supplementary Figure S2).

MATERIALS AND METHODS

Preparation of growth substrates

Industrial alloys (McMaster-Carr, Robbinsville, NJ, USA) were polished mechanically with commercial metal polish (Iosso, Elk Grove, IL, USA). Seeded and templated substrates were prepared by thermal annealing of ZnO sol-gel films, as previously reported³². The ZnO sol-gel was prepared by hydrolyzing Zn acetate dihydrate (Sigma-Aldrich, St. Louis, MO, USA, >98%) in a 96 wt% 2-methoxyethanol (Sigma-Aldrich, anhydrous, 99.8%) and 4 wt% ethanolamine (Sigma-Aldrich) solution by stirring at room temperature for 12 hours. All reagents were used as received. The sol was filtered through a 0.2 μm Nylon filter and spin-cast at 4 k rpm onto solvent- and O₂ plasma-cleaned silicon wafers. After casting, the wafers were directly transferred to a hotplate at 200 °C for 1 hour.

Preparation of micelle templates

PS-*b*-P4VP block copolymers (BCPs; $M_{n,PS}/M_{n,P4VP} = 41 \text{ kDa}/24 \text{ kDa}$, $235 \text{ kDa}/23 \text{ kDa}$, and $188 \text{ kDa}/96 \text{ kDa}$) from Polymer Source, Inc. (Dorval, Quebec, Canada) (PDI 1.1–1.2) were dissolved in toluene to 0.5 wt% polymer for by stirring for 5–7 hours at room temperature. Polymers were used as received. The solutions were then left overnight (8–10 hours) in an oven at 70 °C to decrease polydispersity in the size and shape of the micelles. Solutions were cast at 2 K–2.5 K rpm onto ZnO-seeded substrates to form a monolayer. The growth was performed within 2 hours of casting.

Preparation of 3D substrates

The silicon micropatterning-based 3D structures were prepared through the seeding and templating of a micropatterned silicon sample with 84 K–17.5 K BCP. The multitextured block structure discussed below was prepared by placing a transmission electron microscopy grid (Hartfield, Pennsylvania, USA) rough-side-up in a thin layer of SU-8 (MicroChem, Westborough, MA, USA), which was softened at elevated temperature to adhere to the grid before UV exposure through the glass substrate and post-exposure bake. The entire structure was then coated with seed solution before growth. Other substrates for producing the 3D structures were prepared through seeded or unseeded growth of machined molds as specified in the text.

Growth of ZnO nanowire forests

The hydrothermal ZnO nanowire growth medium was prepared by dissolving 0.00625 M Zn acetate dihydrate (Sigma-Aldrich, >98%) and 0.0250 M hexamethylenetetramine (Sigma-Aldrich, >99%) in a solution of deionized (DI) water and (in the case of BCP-templating) acetone, with acetone added to 5–25 vol% of water. All reagents were used as received. Substrates, prepared as described above, were taped to a glass slide right-side-down using Kapton tape and submerged in a petri dish containing the growth solution held at 90 °C. The glass slide supported the substrate by leaning against the sidewall of the petri dish. The reaction proceeded for 10–30 min, depending on desired nanorod length, and was promptly removed from solution and rinsed with DI water. For the alternative zinc nitrate (ZnNO₃)-based protocol described below, 0.020 M of ZnNO₃ hexahydrate and 0.20 M ammonium hydroxide in DI water solution for 6 hours at 95 °C was used instead.

Forming of BMG nanostructures

Thermoplastic forming was conducted in an Instron (Norwood, MA, USA) device with heated platens. In all cases, samples were allowed to reach the platen temperature by 30 s of contact without load. Initial disks of the Pt-BMG were generated by forming at a 10 kN min⁻¹ constant loading rate for 6 s from cylindrical ingots that were approximately 2.5 mm in height and diameter, at $275 \pm 5 \text{ }^\circ\text{C}$, in the supercooled liquid regime ($T_g = 235 \text{ }^\circ\text{C}$, $T_x = 305 \text{ }^\circ\text{C}$)³³. These disks were then placed in contact with the nanostructured mold and formed through 3 min of a 1.5 kN min⁻¹ applied load. Structures were then removed mechanically and the ZnO was etched by >1 hour immersion in 0.1 M acetic acid (diluted from Sigma Aldrich, >99%), with the solution exchanged for fresh 0.1 M acetic acid and then DI water to prevent precipitation of the ZnO.

Characterization of structures

Nanostructures were imaged by high-resolution scanning electron microscopy in a Hitachi (Schaumburg, IL, USA) SU-70 scanning electron microscope with a 5 kV accelerating voltage. Reflection spectra were collected using a white light source through a 0.2 NA lens and an Ocean Optics (Dunedin, FL, USA) S2000 spectrometer. Simulations were performed with COMSOL Multiphysics (COMSOL, Burlington, MA, USA) finite element method software. The complex optical constants for ZnO were taken from tabulated values³⁴, and the values for the BMG were determined with a J. A. Woollam Co. (Lincoln, NE, USA) M-2000D spectroscopic ellipsometer (Supplementary Figure S6b).

RESULTS AND DISCUSSION

BMG structural tuning by ZnO growth conditions

The efficacy of this technique relies on the ability to controllably generate desired morphologies on targeted surfaces. Although hydrothermal growth of ZnO can be performed on almost any surface by deposition of seeds, most typically by sol-gel casting^{26,35}, it can also occur directly from several metallic surfaces that permit nucleation from a bare surface, including alloys. The nature of these growth surfaces is one of the methods of tuning the final morphology of the ZnO nanostructures. Of the potential surfaces, we focused on mold materials usable for macro/micromachining. These included sol-seeded silicon and three common industrial alloys: 353 (~36% Zn) brass, 260 (~30% Zn) brass, and 2024 aluminum (<0.5% Zn). The ability to grow ZnO on brass arises from its Zn content²⁵, whereas the presence of aluminum has been shown to initiate the growth of one dimensional (1D) ZnO nanosheets²⁷. As an additional means of control, we also utilized controlled-density ZnO arrays prepared from growth on sol-seeded silicon substrates templated through BCP micelles, a method recently developed by our group³². BMG disks were then formed in their supercooled liquid state against the ZnO-coated surfaces in a heated press at a constant loading rate. Photographs and electron micrographs of representative selections of ZnO generated on 353 brass, 2024 aluminum, and two varieties of BCP-templated seeded silicon and resultant nanostructured BMG forms are shown in Figure 2, with additional samples shown in Supplementary Figure S3. These results were highly reproducible for multiple samples and even across different alloy systems, as shown in Supplementary Figure S2. The ZnO structures consist of nanorods with varying diameters from 20 to 100 nm and, from aluminum, nanosheet networks with spatial periodicity of 250–500 nm.

The nanoscale morphologies of both the sacrificial template-embedded-BMG (pre-rinse) and the rinsed BMG porous surface varied greatly depending on the starting morphology. After pressing but before rinsing, the BMG samples generally exhibited

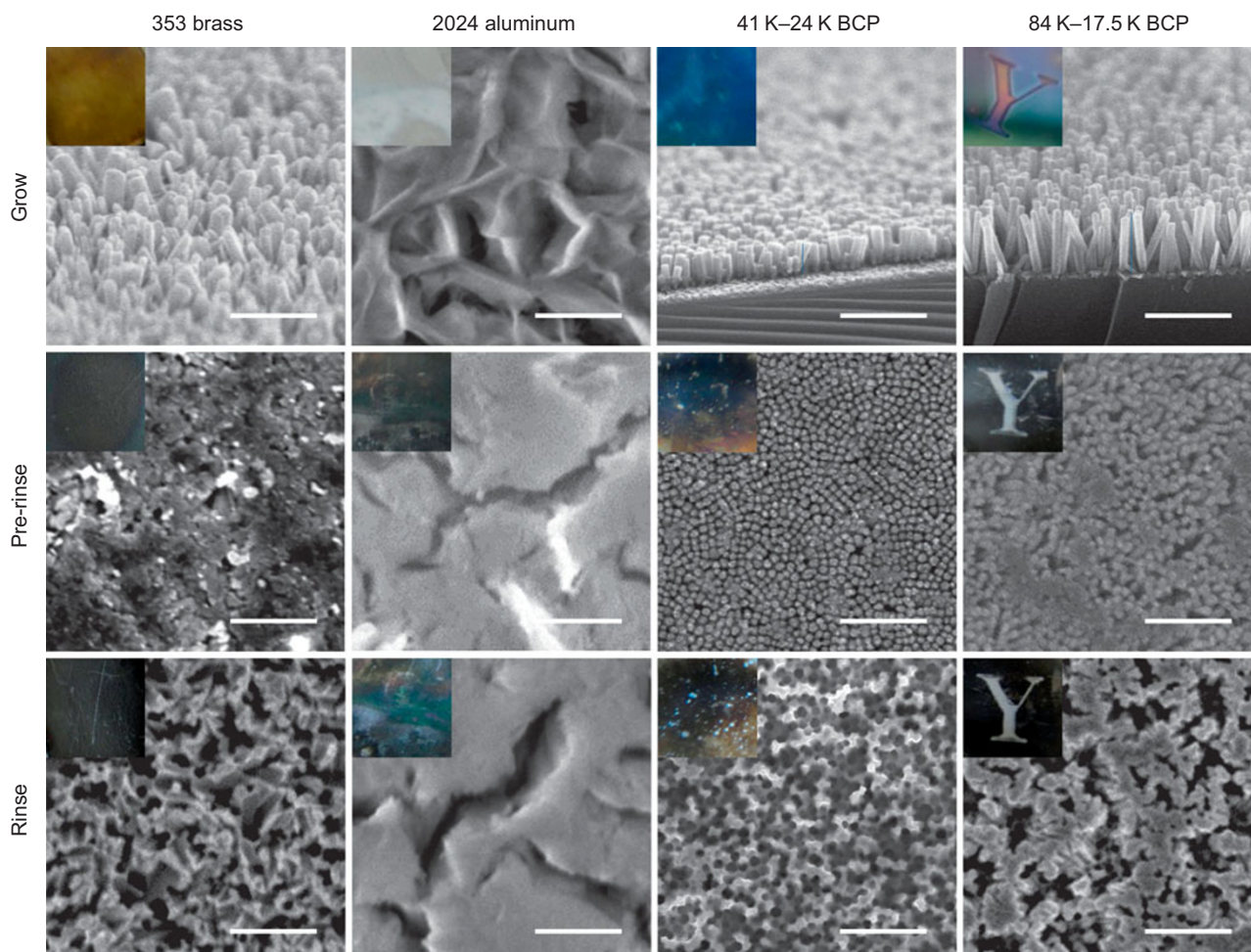


Figure 2 Photographs and nanoscale features of templates and resultant structures. SEM images of four characteristic mold-structured BMG sets (molds formed from ZnO arrays grown on 353 brass, 2024 aluminum, and seeded silicon templated with 41 K–24 K and 84 K–17.5 K BCP micelles; insets demonstrate the nanoscale morphology of the molds, detached structure pre-rinsing, and structure after acid rinse. The 84 K–17.5 K micelle-templated mold contains a laser-patterned ‘Y’ feature. BMG disks are ~8 mm in diameter. All scale bars are 500 nm. Templates, other than aluminum, are imaged at a 45° tilt. Inset field of view is 4–6 mm.

relatively featureless surface morphologies. However, discrete embedded nanorods slightly protruding from the surface were uniquely observed for BMG surfaces patterned using ZnO produced by BCP-templating. These nanorod-embedded metallic surfaces represent a potentially useful nanocomposite material, in which the length, periodicity, and electronic properties of the semiconducting nanomaterial could be engineered to provide optoelectronic or other functional properties.

By contrast, the post-rinse samples showed a wide variety of porous morphologies. Features that arose from the dense ZnO of the seeded silicon and 260 brass (Supplementary Figure S3) or the spatially controlled ZnO grown on 41 K–24 K micellar templates led to highly ordered sub-100 nm textures, whereas the features of the 353 brass led to more random, deeper morphologies, and those of the 2024 aluminum led to web-like morphology. These structures are not direct inversions of the ZnO structure. For example, when grown from seeded silicon, ZnO nanostructures have high aspect ratios and bunch due to mechanical buckling induced by the highly viscous nature of the supercooled BMG liquid during forming. Importantly, the non-slip nature of the BMG forming leads to localization of these mechanical effects, and as a result there is no fracture or dragging of the ZnO nanostructures. This effect is highlighted by the

change in color at the edges of the samples, as shown in photographs in Figure 2 inset, where the magnitude and rate of shear of the BMG flow increases, resulting in radially flattened ZnO and, thereby, BMG structures (Supplementary Figure S4).

Despite the stochastic origin of the features, deliberate tuning of these highly repeatable patterns may be performed. Figure 3 demonstrates modification of the surface structure achieved through the tuning of various processing parameters. Taking seeded silicon as a starting point for a high-Zn surface (Figure 3a), this initial morphology is ‘pore-like,’ i.e., holes in a continuous metallic top surface, with a dense structure. Such morphologies are highly similar to those that have recently been utilized for controlling optical properties and wetting in polymer systems, whereby the geometry was shown to give superior mechanical robustness due to the lack of buckling deformation under loading³⁶. By employing BCP templating, the ZnO rod spacing was increased (Figure 3b–d), leading to distribution of the pores until, with the sparsest 235 K–23 K template (Figure 3d), the individual ZnO imprints were resolved. By changing the seed material from sol-gel ZnO to a Zn alloy, the distribution of surface-active seed sites became less uniform, leading to a dispersion of rod sizes and spacings. As a result, pore sizes in a high-Zn brass (353; Figure 3e) reflected individual features of

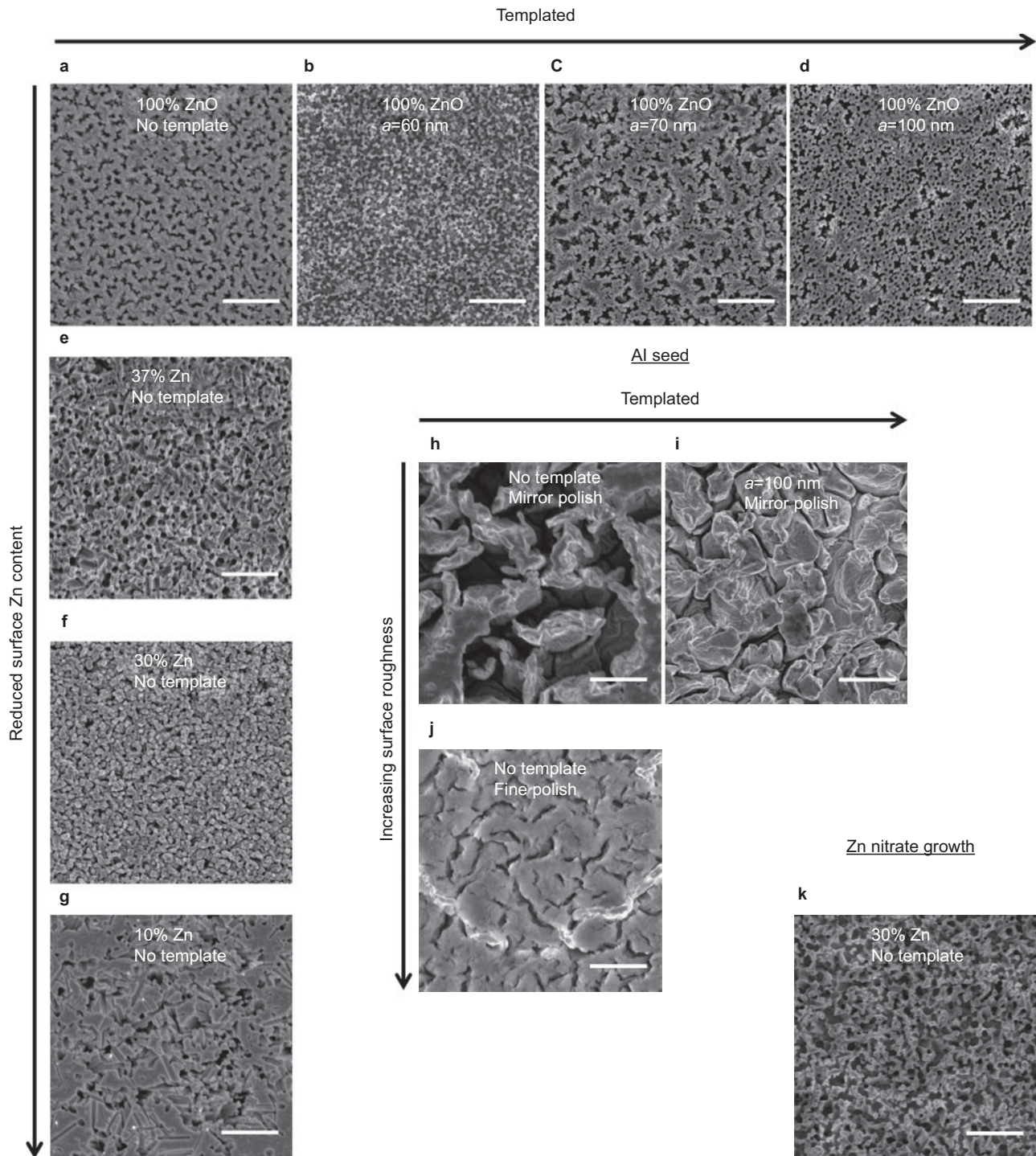


Figure 3 Systematic variation of BMG morphology with growth parameters. (a–d) Variation due to use of BCP template on ZnO seeded surfaces, with effective lattice parameter of the template indicated for (b) 41 K–24 K, (c) 84 K–17.5 K, and (d) 235 K–23 K. (a, e–g) Variation of surface Zn content, with surface content indicated for (a) the ZnO seeded surface, (e) 353 brass, (f) 260 brass, and (g) 220 bronze. (h–j) Structures based on growth from 2024 aluminum with a starting point of (h) mirror polished alloy, through (i) use of a 235 K–23 K template and by (j) varying polish from mirror to fine using 1200 grit paper wheel. (k) Structures fabricated through use of a different ZnO growth protocol involving ZnNO_3 . Scale bars are 1 μm .

higher-diameter rods. Low-Zn brass (220, Figure 3f) generated very thin ZnO rods, which collapsed easily, generating ‘pillar-like’ geometries, i.e., discrete arrays of metallic features. To test the limits of method, an additional sample was made using low-Zn bronze (220, ~10% Zn; Figure 3g) that produced non-uniform

features because the surface concentration of Zn became so low that it varied greatly from grain to grain. Aluminum-based seeding was also tunable, as shown in Figure 3h–j, by the changes in the morphology from pore-like to pillar-like from the use of BCP templating and by the generation of shallower

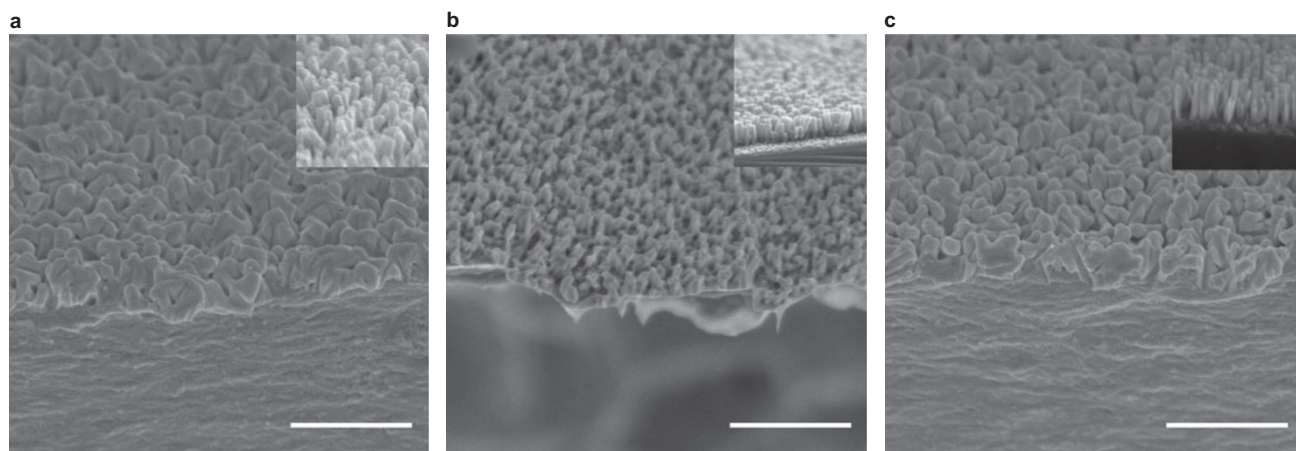


Figure 4 SEM images at a 45° tilt of fractured cross-sections of three representative samples, (a) a 353 brass and (b) 41 K–24 K BCP- and (c) 235 K–23 K BCP-templated samples, with ZnO structures shown in insets. The feature depths are ~350 nm, ~250 nm, and ~500 nm, which is on the order of the feature height as observed by comparison with the same-scale ZnO insets. Scale bars are 1 μm .

features from surface roughening. Finally, the growth of ZnO is well known to be highly sensitive to parameters such as the bath temperature and growth medium. Figure 3k shows morphology resulting from growth of ZnO on 260 brass using a different, ZnNO_3 -based protocol³⁷. Here, the morphology looks very similar to the 353 brass, but on a larger length scale, with 50–75 nm pores.

Cross-sectional imaging reveals that penetration of the nanostructures is on the order of the full structure height (Figure 4), resulting in aspect ratios of up to 5; although this is not a fundamental limit, aspect ratios are limited by the structural buckling. Despite being greater than what can be obtained through soft replica nanoimprinting, it is clear that the aspect ratios obtained through this method do not set any records; aspect ratios have exceeded 50 for single-use AAO mold imprinting of BMG⁶ and 20 for polymer imprinting with reusable diamond molds³⁸. However, the scalability of these structures is much greater because they can be easily regrown and detach instantaneously after rapid cooling without the need for a carefully optimized 30-min cooling procedure, which is required in the polymeric case. Furthermore, the compatibility of this method with complex macro/microarchitectures provides an advantage over other techniques.

Generating 3D hierarchical architectures

When compared to existing methods for producing multiscale nanopatterned metals, such as laser ablation^{12,13} and formable systems, including consecutive imprinting³⁹ or imprinting and photolithography⁴⁰, the principle benefits of the technique described here, beyond the ability to tune the morphology, are the low cost and facile nature by which multiscale patterning is enabled. The ability to produce complexly shaped 3D architectures while maintaining the surface structure with high fidelity leads to immense flexibility; it allows for texturing within a superstructure that is defined by a structured micromold. This texturing includes stochastic patterns (Figure 5a–f) such as those demonstrated with (small-to-large characteristic length) seeded sintered alumina, seeded ground glass, and unseeded ground 260 brass, where the growth is able to follow abrupt changes in morphological orientation. This method is useful for producing structures with multilevel roughness similar to those produced by laser ablation. This method also presents a route to economically produce biomimetic, hierarchical architectures similar to those present on lotus leaves or butterfly wings without requiring top-

down lithography; this is accomplished by using only scalable manufacturing processes, such as grinding or shot-peening.

For many applications, it is more significant that the sacrificial template process can be applied to highly deterministic patterns (Figure 5g–j), such as macroscopically machined 353 brass or seeded micropatterned silicon pores. These deterministic structures show a wide range of possible designer geometries on multiple scales, including sharp angles, vertical sidewalls, and curved surfaces. Furthermore, the sensitivity of ZnO growth to the nature of the substrate provides an additional level of control to both stochastic and deterministic structures. Figure 5k and l shows an array of multiscale structures with four distinct morphologies (rough trenches, non-textured sidewalls, densely nanotextured edges, and sparse tops) over a distance of 2 μm , corresponding to growth on three different surface and seed morphologies. This simple demonstration shows how deliberate mold fabrication methods (e.g., varying composition, roughness, and presence of a template) can be used to tune the resultant ZnO structures on the same surface to create spatially varying properties.

These capabilities enable application to a wide range of macroscale and microscale devices, including those already generated in BMGs, such as shell⁴¹ and MEMS⁴² resonators, blow-molded consumer components⁵, and electrochemical fuel cells⁹. Future applications may include medical implant devices similar to the multiscale stent architecture demonstrated in Figure 1. Additionally, the highly scalable nature of sacrificial imprint patterning of deterministic structures enables generation of multiscale structures over large areas, as shown in Figure 6, by the patterning of a centimeter-scale honeycomb grid using a seeded micropatterned silicon mold.

Optical properties of nanoporous and surface composite BMGs

With the capability of producing tunable nanoscale features on a metallic surface, the utility of this new method needs to be demonstrated by the generation of desirable surface properties and tuned variations sufficient to produce detectable shifts in these properties. We have quantified such control over optical properties, which can be utilized for tunable optical absorption and surface enhanced Raman spectroscopy; however, it can be expected that other surface properties will also be affected, including surface wetting, friction, and biocompatibility.

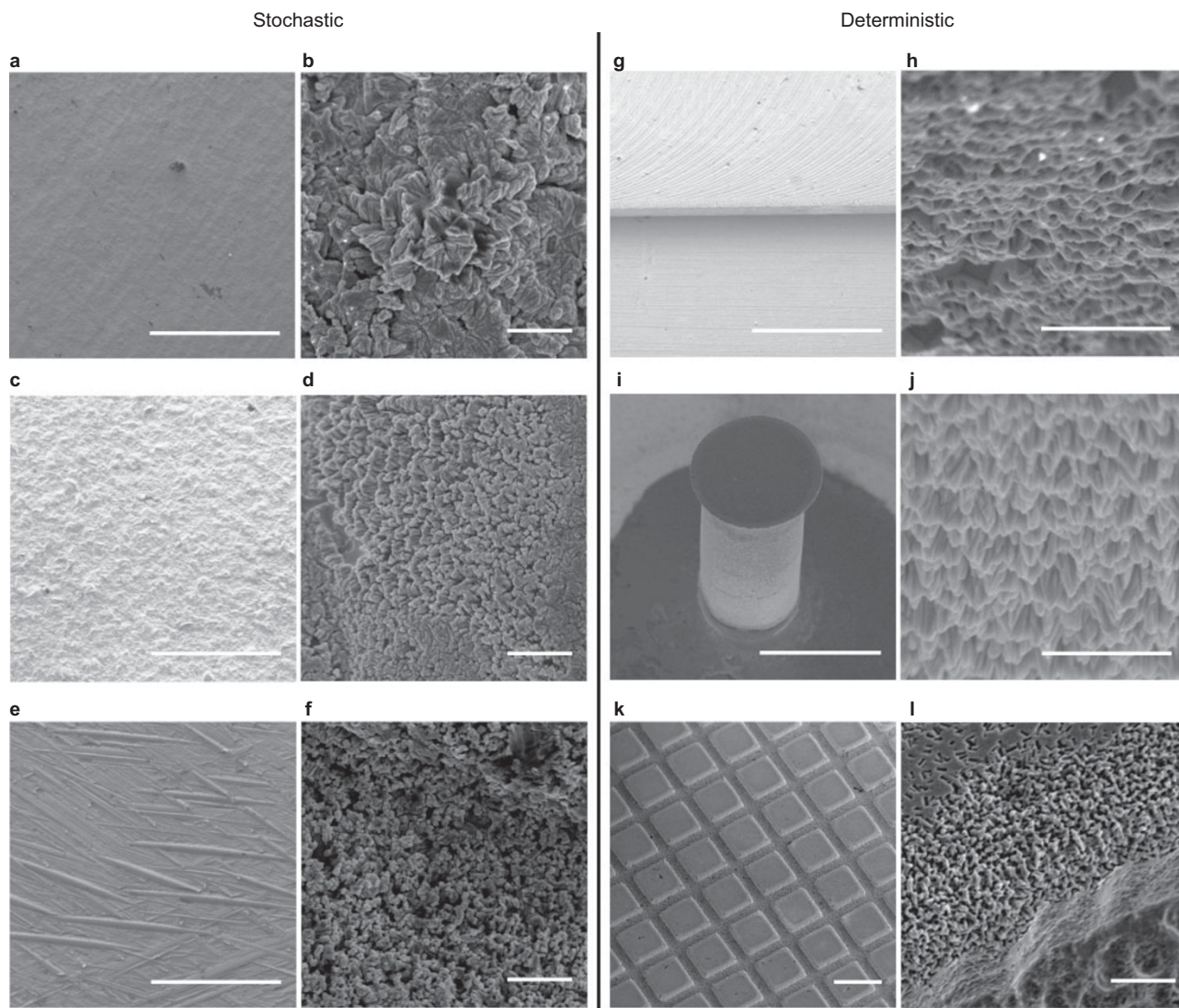


Figure 5 Low (left) and high (right) magnification images of multiscale BMG structures. (a–j) 3D, multiscale BMG structures grown through the sacrificial templating process on the stochastic templates of (a, b) seeded sintered alumina, (c, d) seeded ground glass, and (e, f) unseeded ground 260 brass and the deterministic templates of (g, h) unseeded machined 353 brass and (i, j) seeded, micropatterned Si pillar mold. The replication of the complex topography demonstrates the ability to pattern nearly arbitrarily. (k, l) Multiscale and multitexture structure produced by forming against a seeded TEM grid embedded in epoxy. Each feature in the resulting array possesses rough trenches, non-textured sidewalls, densely nanotextured edges, and sparse tops, showing the rapid rate at which the morphology can be spatially switched by tuning the growth substrate. (g–l) Imaged at a 30° tilt. The scale bars in (a, c, and e) are 1 mm, the scale bars in (g, i, and k) are 100 μm , and the scale bars in (b, d, f, h, j, and l) are 1 μm .

Microreflectometry was employed to quantify the optical features of the BMG and ZnO-embedded BMG surfaces. Figure 7a shows the experimental and simulated direct-incidence reflection spectrum of several characteristic samples. In general, samples were observed to possess broadband absorption, with increasing reflectivity at long wavelengths. Coloration was observed in both the dense samples with the smallest features (e.g., 41 K–24 K BCP-templated) and also the sparse samples with larger features (e.g., 2024 aluminum-templated). Interestingly, the color was only observed in the dense patterns before rinsing and was not iridescent (Supplementary Figure S5), whereas it was most strongly observed in the sparse samples after removal of the ZnO and was iridescent.

These coloration trends can be predicted through finite-element method simulations (details in Supplementary

information). They arise from two different plasmonic waveguide effects, with the key feature being the amount of optical intensity that is in the lossy metallic matrix. When the matrix is very thin, the dominant optical mode travels within the walls, analogous to a 1D insulator-metal-insulator (IMI) waveguide (Figure 7b)⁴³. The guided mode can be seen in the simulated color map of the magnitude of the optical electric field as high intensity in the thinnest portion of the metal matrix. In this case, absorption is *reduced* by incorporation of dielectric material due to the reduction of confinement within the walls when the magnitudes of the complex optical functions approach one another. This primarily occurs at low wavelengths where the metal's optical function (Supplementary Figure S6b) is closest to air/ZnO and is demonstrated in the simulation by broadening into the dielectric region and decrease in relative intensity of the guided mode.

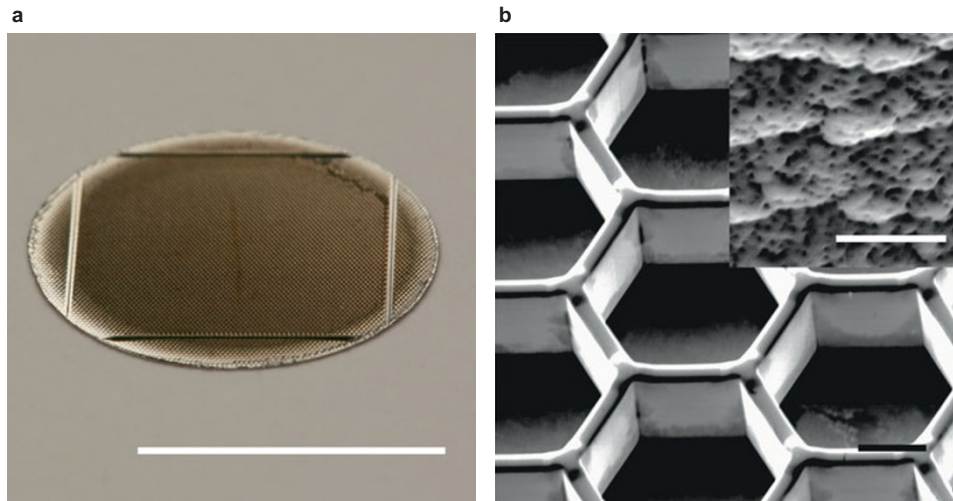


Figure 6 Large multiscale lattice structure. (a) Photograph of centimeter-scale component. (b) SEM image of the lattice with high magnification inset. The scale bar in (a) is 1 cm, and the scale bars in (b) are 50 μm in the main figure and 500 nm in the inset.

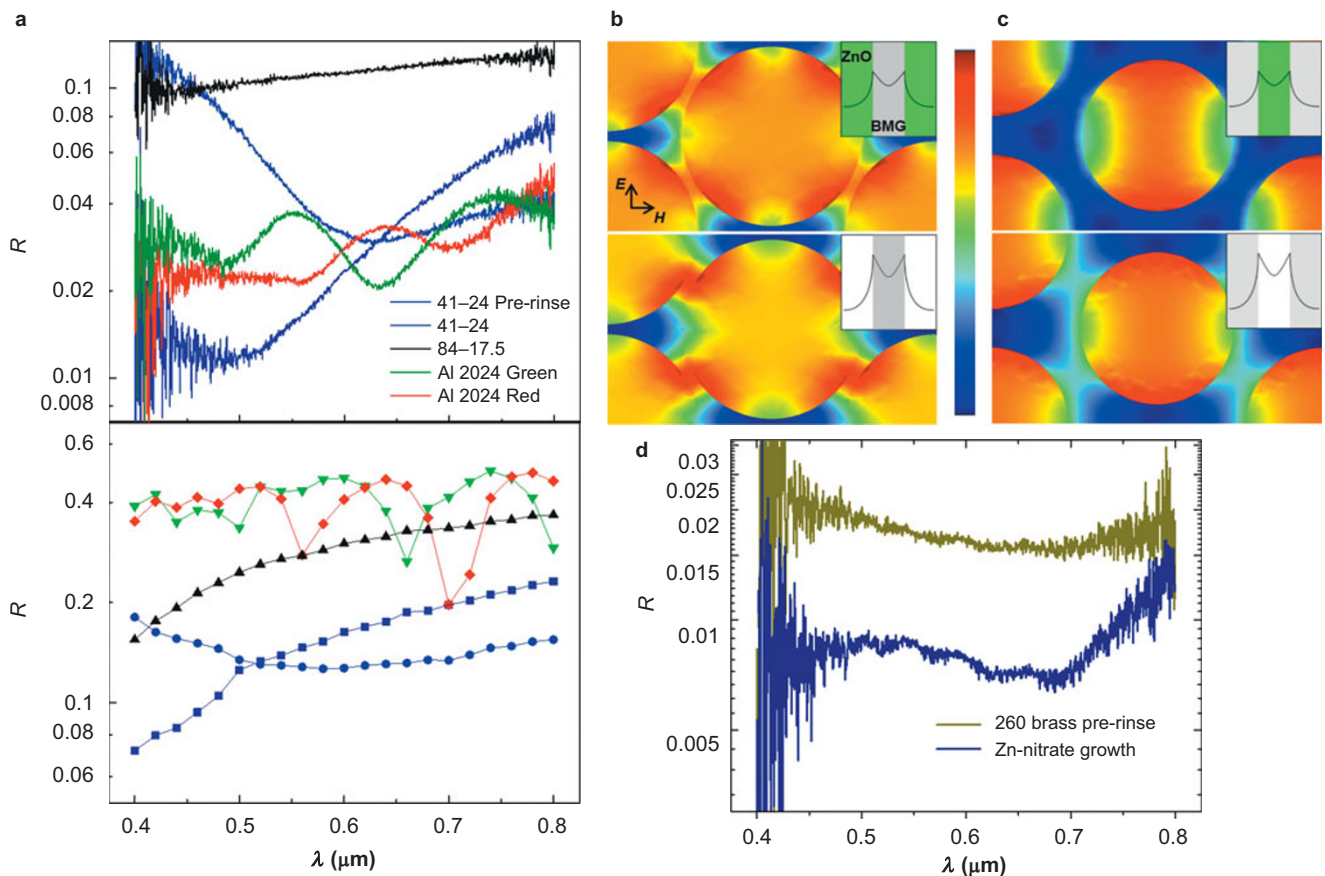


Figure 7 Optical characterization of characteristic nanopatterns. (a) Top: Microreflectometry results of 41 K-24 K BCP-templated samples pre- (light blue trace) and post-rinsing (dark blue trace), a rinsed 84 K-17.5 K BCP-templated sample (black trace), and a rinsed 2024 aluminum-templated sample (red and green traces corresponding to red and green regions of the sample, shown in Figure 2). Bottom: Finite-element simulations of these samples. The BCP-templated samples were modeled as hexagonal lattices of 3D cylinders, whereas the aluminum sample was modeled as 2D square slits. (b) and (c) Simulated, normalized xy-slices of electrical field magnitude just below the sample surface. (b) Intensity maps taken at the maximum reflectivity of the 41 K-24 K BCP-templated, detached sample with 200 nm rod height ($\lambda = 400$ nm) with (top) and without (bottom) ZnO in the pore. The mechanism of these thin-walled samples is closest to that of an IMI waveguide, as illustrated in insets. (c) Intensity maps for the 84 K-17.5 K BCP-templated sample with 400 nm rod height at $\lambda = 500$ nm with (top) and without (bottom) ZnO in the pore. The mechanism of these thick-walled samples is closest to that of a MIM waveguide, as illustrated in insets. The rod-rod distance is 57 nm for (b) and 200 nm for (c). Further details are provided in the Supplementary information. (d) Microreflectometry results of two highly absorbing morphologies generated through two different ZnO growth protocols: (i) a surface nanocomposite from the Zn acetate-based growth used for a majority of the samples and (ii) a nanostructured BMG surface from a ZnNO_3 -based protocol.

As the walls of the metal matrix thicken, the system is better characterized as a distribution of thin metal-insulator-metal (MIM) waveguides (Figure 7c)⁴⁴, with the center of the mode in the ZnO. This can be observed in the simulated color map of the magnitude of the optical electric field through most of the intensity migrating to the dielectric pores. In this case, reduction of confinement by the presence of ZnO leads to more of the intensity being contained in the metal and thus an increase of absorption (see the results for 84 K–17.5 K BCP-templated detached sample in Supplementary Figure S7). As these features become increasingly sparse and approach in-plane spacings on the order of optical wavelengths, such as in the Al-templated samples (Supplementary Figure S8), the number of guided modes in the visible spectrum increases. This leads to coloration that is strongly dependent on the characteristic period of the features, much as with any grating-like structure.

From this mechanism, it is possible to impart both structural color, as shown above, and also highly absorbent surfaces. Figure 7d shows two champion absorbing structures, both fabricated from 260 brass: (i) a surface nanocomposite fabricated using the Zn acetate growth employed in the majority of samples and (ii) a BMG-rinsed structure using larger ZnNO₃-based morphologies (shown in Figure 3k). These structures exhibit broadband visible reflectivities below 3% and are generated without additional seeding or spin coating in a parallel process, providing a highly economical route to black metal surfaces that could be applied in the future to multiscale structures.

CONCLUSION

We have demonstrated a scalable and economical method for the fabrication of nanostructured BMG surfaces that overcomes the limitations of current nanostructure fabrication techniques. Specifically, ZnO structures were utilized as a versatile sacrificial template for the structuring of BMGs formed in the supercooled liquid state, allowing for imprinting of reentrant nanostructures over a millimeter-scale area without surface treatment and with rapid detachment. The resulting structures demonstrated a range of possible morphologies controlled by the growth parameters of ZnO in model 2D and 3D geometries. The demonstrated method represents a practically viable method of nanotexturing metal surfaces, with demonstrated tuning of the resulting optical properties. Utilizing these structures, tuning and study of the bio-manipulation, adhesion, and tribological properties of nanotextured surfaces can be carried out. Furthermore, the preservation of embedded nanostructures opens up considerable possibilities for a variety of nanocomposites beyond ZnO. In this way, 3D metallic structures with surface properties determined by the nature and arrangement of the sacrificial nanomaterials would allow for a nanoscale analog of chemical functionalization that would incorporate both surface chemistry and structure.

ACKNOWLEDGEMENTS

This work was supported by NSF MRSEC DMR-1119826 and ONR YIP award N000141210657. C.I.P. acknowledges financial support from the NSF Graduate Research Fellowship Program (GRFP). Facility use was supported by YINQE. The authors gratefully acknowledge Dr. S. Sohn for assistance in BMG alloy synthesis, Y. Rokhlenko for her assistance in machining, and Dr. S. Kooi (MIT) for his assistance in ellipsometry measurements.

COMPETING INTERESTS

The authors declare no conflicts of interest.

REFERENCES

- Greer AL. Metallic glasses. *Science* 1995; **267**: 1947–1953.
- Greer AL. Metallic glasses...on the threshold. *Materials Today* 2009; **12**: 14–22.
- Chu JP, Wijaya H, Wu CW et al. Nanoimprint of gratings on a bulk metallic glass. *Applied Physics Letters* 2007; **90**: 034101.
- Schroers J. Bulk metallic glasses. *Physics Today* 2013; **66**: 32–37.
- Schroers J, Hodges TM, Kumar G et al. Thermoplastic blow molding of metals. *Materials Today* 2011; **14**: 14–19.
- Kumar G, Tang HX, Schroers J. Nanomoulding with amorphous metals. *Nature* 2009; **457**: 868–872.
- Mukherjee S, Sekol RC, Carmo M et al. Tunable hierarchical metallic-glass nanostructures. *Advanced Functional Materials* 2013; **23**: 2708–2713.
- Carmo M, Sekol RC, Ding S et al. Bulk metallic glass nanowire architecture for electrochemical applications. *ACS Nano* 2011; **5**: 2979–2983.
- Sekol RC, Kumar G, Carmo M et al. Bulk metallic glass micro fuel cell. *Small* 2013; **9**: 2081–2085.
- Arora HS, Xu Q, Xia Z et al. Wettability of nanotextured metallic glass surfaces. *Scripta Materialia* 2013; **69**: 732–735.
- Padmanabhan J, Kinsler ER, Stalter MA et al. Engineering cellular response using nanopatterned bulk metallic glass. *ACS Nano* 2014; **8**: 4366–4375.
- Vorobyev AY, Guo C. Enhanced absorptance of gold following multipulse femtosecond laser ablation. *Physical Review B* 2005; **72**: 195422.
- Vorobyev AY, Guo C. Colorizing metals with femtosecond laser pulses. *Applied Physics Letters* 2008; **92**: 041914.
- Gao H, Hu Y, Xuan Y et al. Large-scale nanoshaping of ultrasoft 3D crystalline metallic structures. *Science* 2014; **346**: 1352–1356.
- Vega AA, Newman RC. Nanoporous metals fabricated through electrochemical dealloying of Ag-Au-Pt with systematic variation of Au:Pt ratio. *Journal of the Electrochemical Society* 2014; **161**: C1–C10.
- Zhang Z, Wang Y, Qi Z et al. Generalized fabrication of nanoporous metals (Au, Pd, Pt, Ag, and Cu) through chemical dealloying. *The Journal of Physical Chemistry C* 2009; **113**: 12629–12636.
- Yu J, Ding Y, Xu C et al. Nanoporous metals by dealloying multicomponent metallic glasses. *Chemistry of Materials* 2008; **20**: 4548–4550.
- Xu B, Arias F, Brittain ST et al. Making negative poisson's ratio microstructures by soft lithography. *Advanced Materials* 1999; **11**: 1186–1189.
- Hu Z, Gorumlu S, Aksak B et al. Patterning of metallic glasses using polymer templates. *Scripta Materialia* 2015; **108**: 15–18.
- Chen YC, Chu JP, Jang JSC et al. Replication of nano/micro-scale features using bulk metallic glass mold prepared by femtosecond laser and imprint processes. *Journal of Micromechanics and Microengineering* 2013; **23**: 035030.
- Hirai Y, Yoshida S, Takagi N. Defect analysis in thermal nanoimprint lithography. *Journal of Vacuum Science and Technology B* 2003; **21**: 2765–2770.
- Martin J, Martin-González M, Francisco Fernández J et al. Ordered three-dimensional interconnected nanoarchitectures in anodic porous alumina. *Nature Communications* 2014; **5**: doi:10.1038/ncomms6130.
- Wang D, Zhang L, Lee W et al. Novel three-dimensional nanoporous alumina as a template for hierarchical TiO₂ nanotube arrays. *Small* 2013; **9**: 1025–1029.
- Yin A, Guico RS, Xu J. Fabrication of anodic aluminium oxide templates on curved surfaces. *Nanotechnology* 2007; **18**: 035304.
- Muth JT, Vogt DM, Truby RL et al. Embedded 3D printing of strain sensors within highly stretchable elastomers. *Advanced Materials* 2014; **26**: 6307–6312.
- Greene LE, Law M, Tan DH et al. General route to vertical ZnO nanowire arrays using textured ZnO seeds. *Nano Letters* 2005; **5**: 1231–1236.
- Fan , Fang G, Guo S et al. Controllable synthesis of flake-like Al-doped ZnO nanostructures and its application in inverted organic solar cells. *Nanoscale Research Letters* 2011; **6**: 546.
- Liu J, Li Y, Fan H et al. Iron oxide-based nanotube arrays derived from sacrificial template-accelerated hydrolysis: Large-area design and reversible lithium storage. *Chemistry of Materials* 2009; **22**: 212–217.
- Wang J, Du N, Zhang H et al. Large-scale synthesis of SnO₂ nanotube arrays as high-performance anode materials of Li-ion batteries. *Journal of Physical Chemistry C* 2011; **115**: 11302–11305.
- Wang ZL. Zinc oxide nanostructures: Growth, properties and applications. *Journal of Physics: Condensed Matter* 2004; **16**: R829.
- Liu Z, Schroers J. General nanomoulding with bulk metallic glasses. *Nanotechnology* 2015; **26**: 145301.
- Pelligra CI, Huang S, Singer JP et al. Scalable high-fidelity growth of semiconductor nanorod arrays with controlled geometry for photovoltaic devices using block copolymers. *Small* 2014; **10**: 4304–4309.
- Legg BA, Schroers J, Busch R. Thermodynamics, kinetics, and crystallization of Pt_{57.3}Cu_{14.6}Ni_{5.3}O_{22.8} bulk metallic glass. *Acta Materialia* 2007; **55**: 1109–1116.
- Adachi S. The Handbook on Optical Constants of Semiconductors: In Tables and Figures. World Scientific Publishing Co. Pvt. Ltd, Singapore, 2012.
- Vayssieres L. Growth of arrayed nanorods and nanowires of ZnO from aqueous solutions. *Advanced Materials* 2003; **15**: 464–466.

- 36 Kim J-G, Choi HJ, Park K-C *et al*. Multifunctional inverted nanocone arrays for non-wetting, self-cleaning transparent surface with high mechanical robustness. *Small* 2014; **10**: 2487–2494.
- 37 Wen, Wu W, Ding Y *et al*. Seedless synthesis of patterned ZnO nanowire arrays on metal thin films (Au, Ag, Cu, Sn) and their application for flexible electromechanical sensing. *Journal of Materials Chemistry* 2012; **22**: 9469–9476.
- 38 Hirai Y, Yoshida S, Takagi N *et al*. High aspect pattern fabrication by nano imprint lithography using fine diamond mold. *Japanese Journal of Applied Physics* 2003; **42**: 3863.
- 39 Hasan M, Schroers J, Kumar G. Functionalization of metallic glasses through hierarchical patterning. *Nano Letters* 2015; **15**: 963–968.
- 40 Zhang Y, Lin C-T, Yang S. Fabrication of hierarchical pillar arrays from thermoplastic and photosensitive SU-8. *Small* 2010; **6**: 768–775.
- 41 Kanik M, Bordeenithikasem P, Kim D *et al*. Metallic glass hemispherical shell resonators. *Journal of Microelectromechanical Systems* 2015; **24**: 19–28.
- 42 Kanik M, Bordeenithikasem P, Kumar G *et al*. High quality factor metallic glass cantilevers with tunable mechanical properties. *Applied Physics Letters* 2014; **105**: 131911.
- 43 Charbonneau R, Berini P, Berolo E *et al*. Experimental observation of plasmon polariton waves supported by a thin metal film of finite width. *Optics Letters* 2000; **25**: 844–846.
- 44 Zia R, Selker MD, Catrysse PB *et al*. Geometries and materials for subwavelength surface plasmon modes. *Journal of the Optical Society of America A* 2004; **21**: 2442–2446.



This work is licensed under a Creative Commons Attribution 4.0 Unported License. The images or other third party material in this article are included in the article's Creative Commons license, unless indicated otherwise in the credit line; if the material is not included under the Creative Commons license, users will need to obtain permission from the license holder to reproduce the material. To view a copy of this license, visit <http://creativecommons.org/licenses/by/4.0>

Supplementary information for this article can be found on the *Microsystems & Nanoengineering* website (<http://www.nature.com/micronano>).